

Effect of x-ray energy dispersion in digital subtraction imaging at the iodine *K*-edge—A Monte Carlo study

F. Prino^{a)}

Dipartimento di Fisica Sperimentale dell'Università di Torino and INFN, Torino, Italy

C. Ceballos and A. Cabal

CEADEN, Havana, Cuba

A. Sarnelli

Azienda Ospedaliera S. Orsola Malpighi, Bologna, Italy

M. Gambaccini

Dipartimento di Fisica dell'Università di Ferrara and INFN, Ferrara, Italy

L. Ramello

Dipartimento di Scienze e Tecnologie Avanzate dell'Università del Piemonte Orientale and INFN, Alessandria, Italy

(Received 10 May 2007; revised 17 October 2007; accepted for publication 19 October 2007; published 11 December 2007)

The effect of the energy dispersion of a quasi-monochromatic x-ray beam on the performance of a dual-energy x-ray imaging system is studied by means of Monte Carlo simulations using MCNPX (Monte Carlo N-Particle eXtended) version 2.6.0. In particular, the case of subtraction imaging at the iodine *K*-edge, suitable for angiographic imaging application, is investigated. The average energies of the two beams bracketing the iodine *K*-edge are set to the values of 31.2 and 35.6 keV corresponding to the ones obtained with a compact source based on a conventional x-ray tube and a mosaic crystal monochromator. The energy dispersion of the two beams is varied between 0 and 10 keV of full width at half-maximum (FWHM). The signal and signal-to-noise ratio produced in the simulated images by iodine-filled cavities (simulating patient vessels) drilled in a PMMA phantom are studied as a function of the x-ray energy dispersion. The obtained results show that, for the considered energy separation of 4.4 keV, no dramatic deterioration of the image quality is observed with increasing x-ray energy dispersion up to a FWHM of about 2.35 keV. The case of different beam energies is also investigated by means of fast simulations of the phantom absorption. © 2008 American Association of Physicists in Medicine. [DOI: [10.1118/1.2815360](https://doi.org/10.1118/1.2815360)]

Key words: dual-energy x-ray imaging, quasi-monochromatic x-ray beams, MCNP simulations

I. INTRODUCTION

Dual-energy subtraction imaging at the *K*-edge is a promising technique for enhancing the detail visibility in medical examinations which make use of a contrast agent. This imaging technique exploits the sharp rise of the absorption coefficient at the energy of the *K*-edge of a given chemical element present in the contrast medium (e.g., iodine at 33.17 keV or gadolinium at 50.24 keV). Two images are taken after the contrast medium administration at two different energies, one just below and one just above the *K*-edge energy of the involved chemical element. The logarithmic subtraction of the high-energy and low-energy images allows one to obtain a final image where the contrast agent visibility is improved because the background structures are canceled.¹

To date, the application of this technique has been studied mainly for coronary^{2,3} and neurovascular⁴ angiography using iodine or gadolinium as a contrast medium. Applications of subtraction imaging to digital mammography (to detect the angiogenesis associated with breast cancer growth) are also being investigated, using either temporal⁵ or dual-energy⁶ subtraction.

The clinical application of dual-energy imaging has been limited so far by the absence of a suitable dichromatic x-ray source. The monochromatic x-ray beams produced with synchrotron radiation would be the ideal source thanks to the high intensity and the possibility of having the two energies very close to the *K*-edge of the contrast element. However, the high cost and the small number of imaging beam lines available in the world disfavor the use of synchrotrons for widespread clinical application of *K*-edge subtraction imaging.

In the last decade, a compact source which generates quasi-monochromatic beams with a conventional x-ray tube and a mosaic crystal monochromator has been developed.^{7,8} Subtraction imaging at the iodine *K*-edge has been tested in the last few years using this x-ray beam facility, together with silicon strip detectors with single-photon counting capability. The obtained results demonstrated an interesting image quality also for iodine concentrations reduced with respect to normal clinical practice.^{9,10} In the case of coronary angiography application, the aim is to acquire good quality

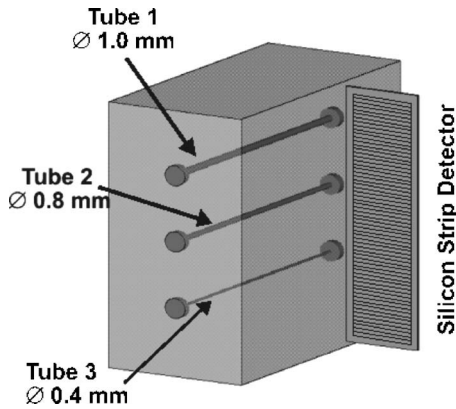


FIG. 1. Scheme of the simulated geometry with the PMMA phantom and the silicon strip detector.

images with the typical iodine concentrations that are obtained with intra-venous injection of the contrast medium, so as to avoid patient catheterization.

With this imaging source, two beams with energies separated by ≈ 4 keV and energy dispersion of the order of 1 keV of Gaussian sigma are obtained. The effect of the larger separation between the two beam energies with respect to the performance obtained at synchrotrons has been recently studied in Refs. 11 and 12, where it is concluded that an energy separation of 4 keV is not a limit for the application of the *K*-edge subtraction technique, provided that enough photon flux can be obtained with the compact x-ray source.

The aim of the present work is to investigate the effect of the energy dispersion of such a quasi-monochromatic beam on the imaging capabilities of the system described above. The x-ray energy dispersion is expressed in this work through its Gaussian width σ_{E_γ} ; hence, the full width at half-maximum (FWHM) results to be $2.35 \cdot \sigma_{E_\gamma}$. The study is based on MCNPX (Ref. 13) simulations, which have proved to be able to reproduce the main features of the imaging system as measured in imaging experiments with phantoms made out of tissue-equivalent materials.^{10,14}

II. MCNPX SIMULATION

The computer simulations have been carried out using the MCNPX (Monte Carlo N-Particle eXtended) version 2.6.0 code. MCNPX is a general-purpose Monte Carlo radiation transport code for modeling the interaction of radiation with matter. MCNPX is designed for transporting all particle types. In previous studies,^{10,14} we used MCNP-4C, which transports only neutrons, photons, and electrons

Fig. 1 shows the simulated phantom and detector geometry. The phantom consists of a PMMA slab ($4 \times 4 \times 2$ cm) containing three iodine-filled cylindrical cavities with diameters of 0.4, 0.8, and 1 mm, respectively. The phantom thickness is uniform, giving rise in the image to a background without structures. The presence of background structures is in fact the main reason for using the *K*-edge subtraction technique, which allows cancellation of them. However, the background cancellation capability has been already studied

in previous papers (see, e.g., Refs. 9 and 10), while the focus of this work is on the study of the visibility of the cavities when increasing the energy dispersion of the beam. Hence, a simpler phantom has been chosen to investigate the effect of nonmonochromatic beams.

The detector is a 384-strip silicon detector in edge-on configuration.^{10,14} The strip pitch and length are $100 \mu\text{m}$ and 10 mm, respectively; the detector thickness is $300 \mu\text{m}$, resulting (in the case of edge-on irradiation) in a pixel size of $100 \times 300 \mu\text{m}^2$ and an active length of 10 mm. The thickness of the inactive region (guard rings+detector edges) upstream from the strips is $765 \mu\text{m}$.

The detector model used has been validated previously against experimental measurements for both *K*-edge subtraction angiography and dual-energy mammography applications.^{10,14} As in the previous cases, each incident photon is tracked until (a) it is totally absorbed within the phantom volume; (b) it is totally absorbed within the detector volume; or (c) it escapes from both of them. A photon is counted by the detector if its energy deposit in the strip active volume exceeds 7 keV, which corresponds to the discriminator threshold used in the single-photon counting electronics of the actual detector for complete noise rejection. The secondary electrons generated by the interaction of the incident photons with either the phantom or the detector are considered to locally deposit their energy and thus are not further transported. The simulation of the interactions is based on the mcplib02 data library that uses ENDF/B-VI (Evaluated Nuclear Data File) cross-section data.

A parallel x-ray beam has been simulated in normal incidence on the phantom's front side. The simulated beam is 4 cm long and $300 \mu\text{m}$ wide, so it covers a fraction of the phantom volume corresponding to the transverse size of the silicon detector in edge-on configuration. It should be pointed out that many issues which could play an important role in practical applications (such as beam divergence, energy gradients, noise in the readout electronics, etc.) are not included in these simulations, which are exclusively meant to study the effect of x-ray energy dispersion and not to give a full and precise description of the actual experimental situation. The energy of the incoming photons has been generated according to a Gaussian distribution. Different simulations have been performed varying the value of the Gaussian width σ_{E_γ} from 0 to 4 keV with 0.5 keV step (corresponding to FWHM values ranging from 0 to 9.4 keV). Finally, for creating the phantom image, 15 profiles have been generated by doing 15 runs for each average energy (31.2 and 35.6 keV) and each σ_{E_γ} value, changing for each profile the starting seed of the random number generator. So, a total of 270 runs per iodine concentration have been made. Three iodine concentrations have been investigated: 92 , 46 , and 23 mg/ml. For every run the histories-per-simulation are 8×10^6 . For each value of energy dispersion a set of profiles without phantom has also been generated and they have been used to apply the flat-field correction in the same way as it is applied to real profiles in order to remove artifacts caused by the pixel-to-pixel variations of the detection efficiency and

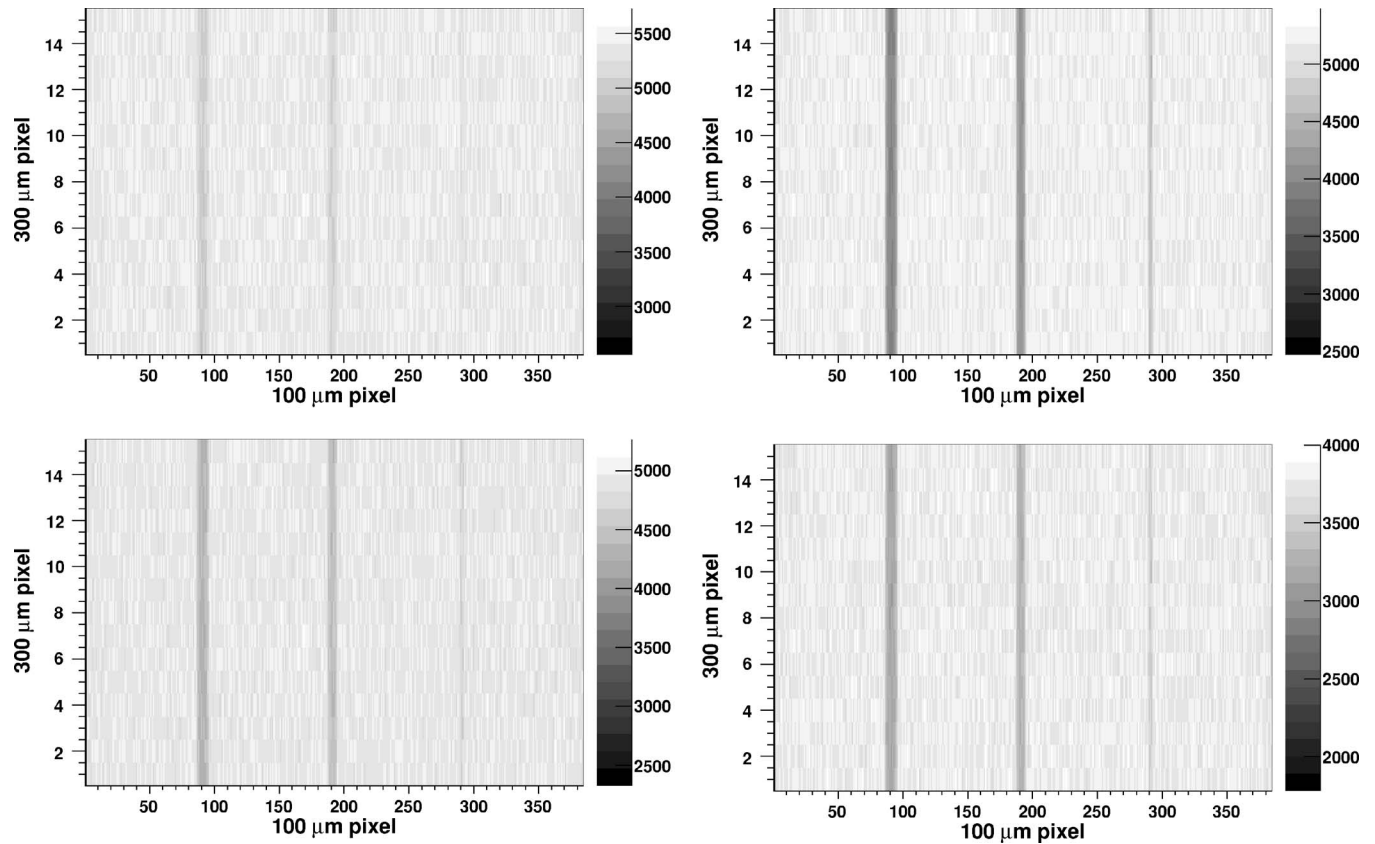


FIG. 2. Simulated images at $\langle E_\gamma \rangle$ of 31.2 keV (left panels) and 35.6 keV (right panels) for σ_{E_γ} values of 1 keV (top panels) and 4 keV (bottom panels), corresponding to FWHM of 2.35 and 9.4 keV, respectively. The iodine concentration is 92 mg/ml.

by the nonuniformity of the radiation field. The simulations have been carried out using a computing cluster consisting of 128 processors (MPIS R1400/600 MHz) from SGI Origin 3800 with a total RAM of 128 GB on IRIX operating system. MCNPX version 2.6.0 has been used on MPI parallel processing.

In the top panels of Fig. 2 the resulting images for beam energies of 31.2 keV (left) and 35.6 keV (right) for $\sigma_{E_\gamma} = 1$ keV and an iodine concentration of 92 mg/ml are displayed. In the bottom panels, the two images in the case of $\sigma_{E_\gamma} = 4$ keV are shown. The pixel size is 100 μm perpendicular to the iodine-filled cavities and 300 μm parallel to the cavities. For $\sigma_{E_\gamma} = 1$ keV the visibility of the iodine details is much better in the high-energy image, as expected from the larger value of the iodine absorption coefficient for energies above the K -edge. In the case of $\sigma_{E_\gamma} = 4$ keV the difference between the two images is much less pronounced. This is due to the fact that in the case of $\sigma_{E_\gamma} = 4$ keV a significant fraction (about 31%) of photons of the low energy beam has an energy higher than the 33.17 keV of the iodine K -edge (and about 27% of the photons of the high-energy beam are below the K -edge). The energy distribution of the x rays in the high and low-energy beams is shown in the left panels of Fig. 3 for the cases of $\sigma_{E_\gamma} = 1$ keV (top) and $\sigma_{E_\gamma} = 4$ keV (bottom). In the right panels of Fig. 3, the corresponding distributions of the iodine absorption coefficient for the two beams are shown. The energy dependence of the

iodine absorption coefficient has been taken from the XCOM (Ref. 15) database. It can be seen that in the case of $\sigma_{E_\gamma} = 1$ keV (top panels) the distributions of the absorption coefficient of the high and low-energy beams are well separated, which is not the case for $\sigma_{E_\gamma} = 4$ keV (bottom). Consequently, the difference between the average iodine absorption coefficient of the two beams is larger for $\sigma_{E_\gamma} = 1$ keV than for $\sigma_{E_\gamma} = 4$ keV, and this is reflected in the different contrast of the iodine-filled cavities in the low and high-energy images of Fig. 2.

III. IMAGE PROCESSING

The low and high-energy images are given by

$$N(E_\pm) = N_0(E_\pm) \exp \left\{ - \sum_i \left[\frac{\mu}{\rho}(E_\pm) \right]_i (\rho t)_i \right\}, \quad (1)$$

where the subscript i denotes the various materials that compose the phantom (iodine and PMMA in our case), $N_0(E_\pm)$ is the number of incident photons in the area defined by an image pixel, μ/ρ is the mass attenuation coefficient of material i at a given energy, ρ is the density, and t the path length in material i . Since the energy separation ($\Delta E = E_+ - E_-$) of the two quasi-monochromatic beams is about 4 keV, the difference between the absorption coefficients of the background structures is not negligible when performing the logarithmic subtraction. This difference would generate a

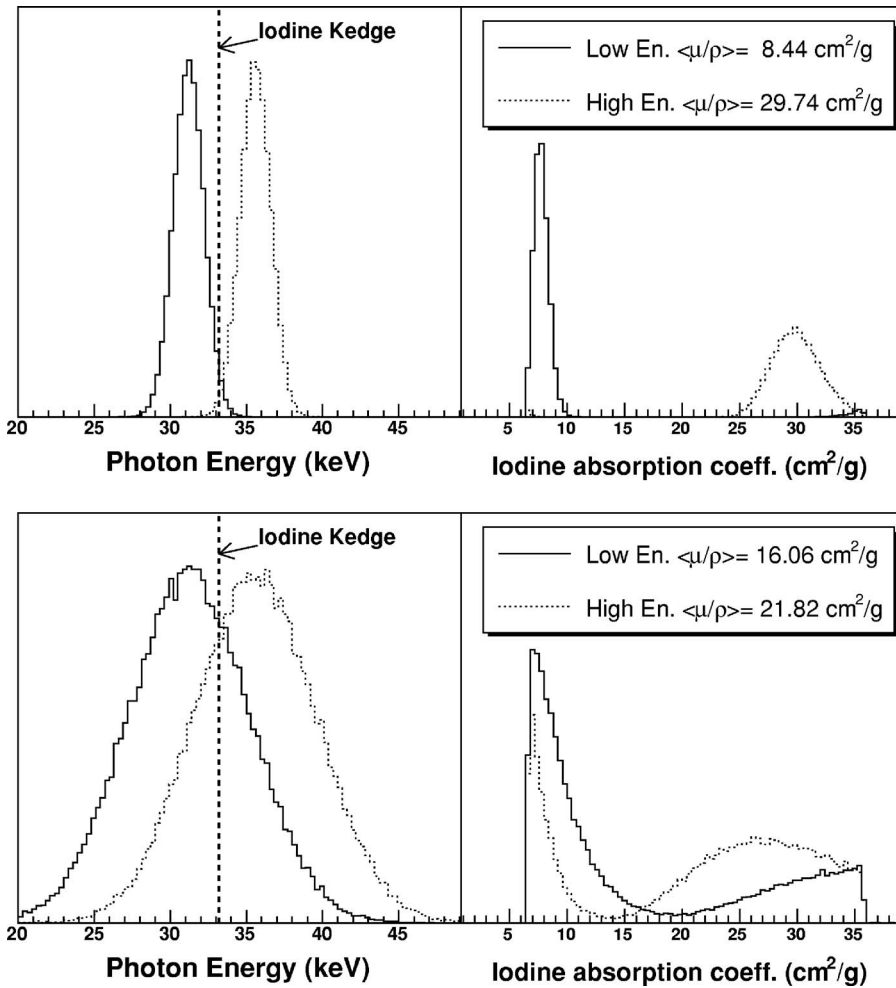


FIG. 3. Energy and iodine absorption coefficient distribution of the photons in the high and low-energy beams for $\sigma_{E_\gamma} = 1$ keV (top) and $\sigma_{E_\gamma} = 4$ keV (bottom), corresponding to FWHM of 2.35 and 9.4 keV, respectively. The values of absorption coefficient as a function of x-ray energy are from the XCOM (Ref. 15) database.

spurious background in the subtracted image due to the incomplete cancellation of the contrast arising from the other materials. The complete cancellation of the background material can be obtained by introducing appropriate weighting coefficients in the logarithmic subtraction, resulting in a composite image H ,

$$H = A \cdot \ln \frac{N_0}{N}(E_+) - B \cdot \ln \frac{N_0}{N}(E_-). \quad (2)$$

For background cancellation, only the ratio A/B is relevant. If the background is composed of one single material (indicated as BKG), like in the case of our phantom, from Eq. (2) the average pixel value in the background regions of the log-subtracted image (H_{BKG}) results to be

$$H_{\text{BKG}} = \left\{ A \cdot \left[\frac{\mu}{\rho}(E_+) \right]_{\text{BKG}} - B \cdot \left[\frac{\mu}{\rho}(E_-) \right]_{\text{BKG}} \right\} (\rho t)_{\text{BKG}}. \quad (3)$$

The background cancellation is obtained for $H_{\text{BKG}} = 0$; hence,

$$\frac{A}{B} = \frac{[\mu/\rho(E_-)]_{\text{BKG}}}{[\mu/\rho(E_+)]_{\text{BKG}}}. \quad (4)$$

In Table I the values of mass attenuation coefficients for some typical tissue-equivalent materials and iodine at the

two energies of interest are reported. It can be seen that the ratio of the coefficients is practically the same for all the considered tissue-equivalent materials (i.e., the background that should be canceled in the resulting image) and very different from that of iodine (i.e., the contrast agent to be isolated).

The values of the weighting coefficients A and B in Eq. (2) can be calculated within the framework of the dual-energy contrast cancellation algorithm,^{17,18} which allows the imaged sample to be decomposed into two basis materials. The basic idea of this method is to describe the x-ray attenuation in a given image pixel as a linear superposition of the

TABLE I. Mass attenuation coefficients of interesting materials (from XCOM, Ref. 15) at the two energies involved in K -edge subtraction angiography.

| Material | $\frac{\mu}{\rho}(31.2 \text{ keV})$ [cm ² /g] | $\frac{\mu}{\rho}(35.6 \text{ keV})$ [cm ² /g] | $\frac{\mu_{31}}{\mu_{35}}$ |
|-------------------------|--|--|-----------------------------|
| Water | 0.3553 | 0.3017 | 1.18 |
| PMMA | 0.2905 | 0.2565 | 1.13 |
| Soft tissue (ICRU-44) | 0.3584 | 0.3033 | 1.18 |
| Bone cortical (ICRU-44) | 1.204 | 0.8700 | 1.38 |
| Iodine | 7.71 | 29.87 | 0.26 |

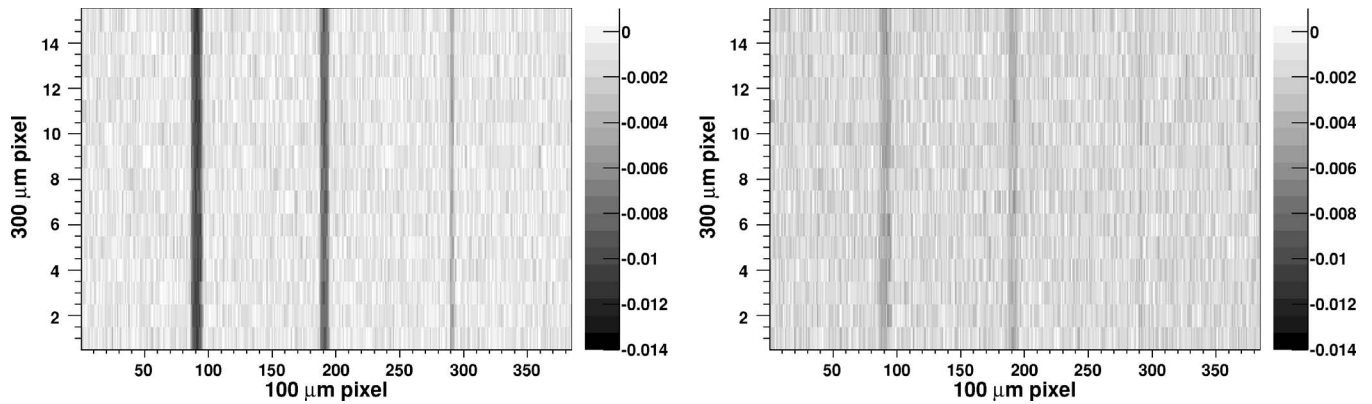


FIG. 4. Logarithmic subtraction of the high and low-energy simulated images of Fig. 2 for iodine concentration of 92 mg/ml and σ_{E_γ} of 1 keV (left panel) and 4 keV (right panel), using iodine and water as basis materials.

contribution of two basis materials X and W . In our case, X is the contrast medium which should be isolated from the “fictitious” element W which comprises all the other (background) materials. In order to have $H = \rho t_X$ (i.e., to preserve in the log-subtracted image the quantitative information about the distribution of the contrast agent mass density) the weighting coefficients A and B must be set to⁹

$$A = \frac{[\mu/\rho(E_-)]_W}{K_0},$$

$$B = \frac{[\mu/\rho(E_+)]_W}{K_0}, \quad (5)$$

with

$$K_0 = \left[\frac{\mu}{\rho}(E_-) \right]_W \cdot \left[\frac{\mu}{\rho}(E_+) \right]_X - \left[\frac{\mu}{\rho}(E_+) \right]_W \cdot \left[\frac{\mu}{\rho}(E_-) \right]_X. \quad (6)$$

In this way, the pixel value in the final image equals the contrast agent mass density ($H = \rho t_{\text{iodine}}$), which is an important feature that allows quantitative measurements on the subtracted image, e.g., in the case of stenosis in angiographic examinations. It should be noted that, even if the signal is proportional (but not equal) to the contrast, the quantitative information on ρt_{iodine} can be recovered by means of a calibration procedure; see, e.g., Ref. 16. In the analyses presented in this paper, water and iodine have been chosen as default “basis” materials in the dual-energy algorithm, following the same choice of Refs. 9, 11, and 12. The resulting values of the weighting coefficients [calculated using Eq. (5) and the absorption coefficients reported in Table I] are therefore $A = 0.0429$ and $B = 0.0364$ (giving a ratio $A/B = 1.18$). As will be discussed in detail in Sec. IV A, the choice of water instead of PMMA as a basis material results in an incomplete cancellation of the PMMA signal (i.e., a nonzero level of the background) in the log-subtracted image due to the difference between the A/B ratios of water and PMMA. For comparison, the results obtained using PMMA and iodine as basis materials (i.e., weighting coefficients $A = 0.0434$ and $B = 0.0383$ with a ratio $A/B = 1.13$) are also presented. Let us

stress that the cancellation of the background (and the signal-to-noise ratio) of the resulting image depends only on the ratio A/B , while the fact that $H = \rho t_{\text{iodine}}$ depends on the actual values of A and B .

The images obtained from the ones in Fig. 2 after logarithmic subtraction using iodine and water as basis materials are shown in Fig. 4. The values of $N_0(E_\pm)$ are extracted from flat-field profiles after proper renormalization. The resulting pixel value in the background (PMMA) pixels is close to zero (≈ -0.001), but not exactly zero because the choice of water instead of PMMA as a basis material results in an incomplete cancellation of the background in the subtracted image.

The quality of the image is evaluated by calculating the values of signal and of signal-to-noise ratio (SNR). The signal S produced by a tube filled with iodine is defined as the difference between the peak and the background pixel values and is averaged over the 15 profiles of the image. The SNR is calculated as the ratio between the signal S produced by the iodine vessel and the background noise (σ_{BKG}),

$$\text{SNR} = \frac{S}{\sigma_{\text{BKG}}}. \quad (7)$$

The noise σ_{BKG} is measured by dividing the regions of the image where the iodine signal is not present into n subimages of area A_{NS} (sampling area for noise). For each subimage an average pixel value X_{sub} is calculated and σ_{BKG} is defined as the standard deviation of the X_{sub} values extracted from the n subimages of area A_{NS} . The size of the sampling area for noise A_{NS} should correspond to the size of the object to be detected. The larger the detail of interest, the larger the sampling area A_{NS} and consequently, the smaller the fluctuations of counts among sampling areas (i.e., the smaller σ_{BKG}).

As an example, the values of SNR characterizing the three iodine-filled cavities of the phantom in the subtracted image of Fig. 4—left ($\sigma_{E_\gamma} = 1$ keV, FWHM = 2.35 keV) are shown in Fig. 5 as a function of the size of the sampling area for noise together with $K \cdot \sqrt{N_{\text{pixels}}}$ fitting functions. It can be seen that the SNR increases when the size of the noise-sampling

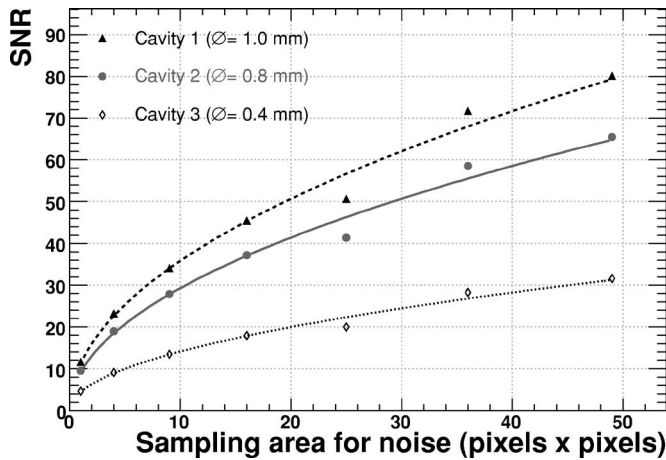


FIG. 5. SNR of a subtracted image (case of iodine concentration of 92 mg/ml and $\sigma_{E_\gamma}=1$ keV) as a function of the number of pixels in the sampling area for noise. Fitting functions $K \cdot \sqrt{N_{\text{pixels}}}$ are also shown.

area increases, and that it follows the expected $\sqrt{N_{\text{pixels}}} \times (\propto \sqrt{A_{\text{NS}}})$ trend. This reflects the better visibility of a larger detail with respect to a small one having the same contrast. As expected, the observed SNR increases with increasing diameter of the tube, i.e., with increasing contrast-medium thickness.

IV. RESULTS

The two important items of background cancellation and detail visibility as a function of the energy smearing of the s-ray beam are discussed separately in the next two subsections. Finally, in the third subsection, the case of different energy separation between the two quasi-monochromatic beams is investigated by means of fast simulations of phantom absorption.

IV.A. Background cancellation

As already pointed out previously, the weighting coefficients A and B in the logarithmic subtraction algorithm should be tuned to cancel the signal of the background materials in the final image. Hence, the pixel value in the PMMA regions of the phantom should be on average zero. However, the choice of the two basis materials of the dual-energy algorithm does have an influence on the background cancellation. In Fig. 6, the average profiles of the logarithmically subtracted images for two different choices of the basis materials (namely iodine/water and iodine/PMMA) are superimposed. The three plots are for three different values of x-ray energy dispersion, namely 0 keV (left), 1 keV (middle), and 4 keV (right panel). In all cases, the simulated iodine concentration is 92 mg/ml. It can be seen that, when iodine and water are used as basis materials (continuous line), a nonzero level is observed in the background pixels because of residual PMMA signal. On the contrary, in the case of iodine and PMMA as basis materials a complete PMMA cancellation is obtained (as expected), at least for the two lower values of energy dispersion.

A systematic shift of the background level is observed in the subtracted image profiles with $\sigma_{E_\gamma}=4$ keV for both choices of basis materials. The distributions of the background pixel values in the subtracted images are shown in Fig. 7—left for four different values of x-ray energy smearing in the case of iodine/water basis materials. The average value of the background pixels is plotted in Fig. 7—right as a function of the energy dispersion of the beam. For $\sigma_{E_\gamma} \leq 1$ keV the average background value is practically independent of the energy smearing of the photons. For larger values of σ_{E_γ} , the background level shifts systematically away from zero with increasing x-ray energy dispersion. The same trend is observed when iodine and PMMA are used as basis materials. Hence, the background cancellation in the logarithmic subtraction results to be affected by the presence

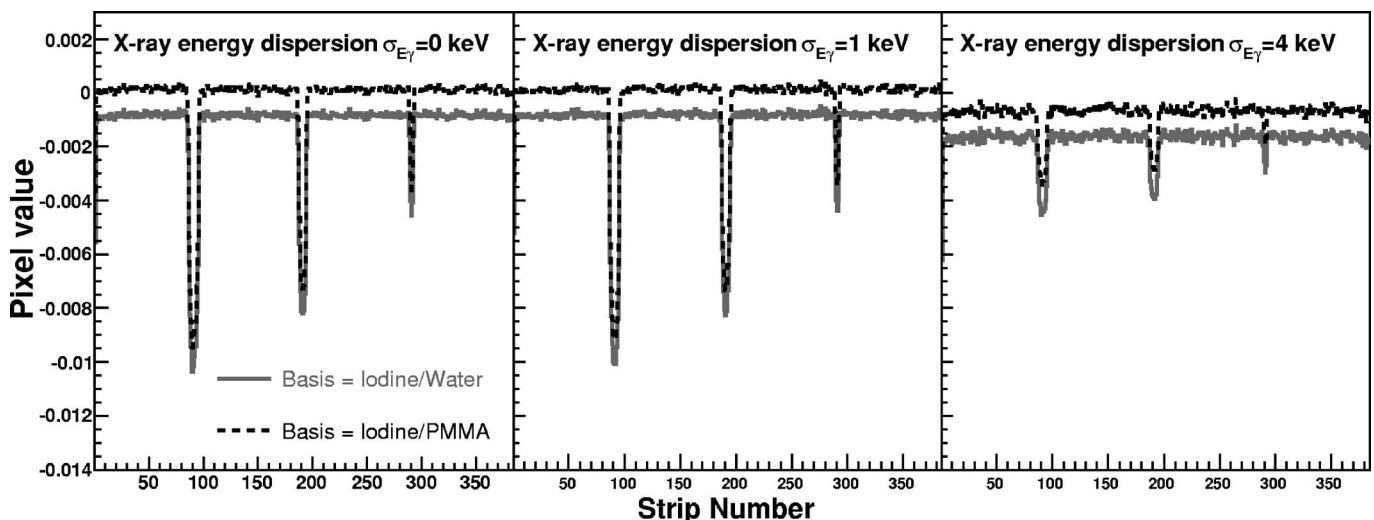


FIG. 6. Average profiles of log-subtracted images for two different choices of basis materials (i.e., weighting coefficients A and B) in the case of iodine concentration of 92 mg/ml and $\sigma_{E_\gamma}=0$ keV (left), 1 keV (middle), and 4 keV (right panel).

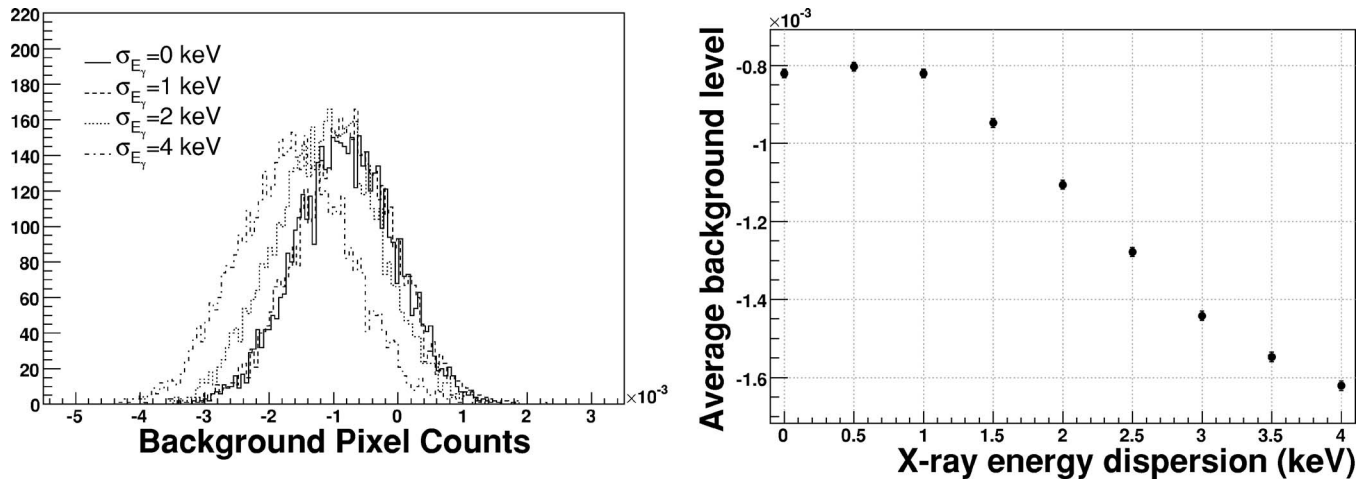


FIG. 7. Left: distribution of the pixel values in the background (PMMA) regions of the log-subtracted image for four different values of x-ray energy dispersion. Right: average background level in the subtracted image as a function of energy dispersion σ_{E_γ} .

of the x-ray energy dispersion only if such dispersion has a Gaussian width larger than ≈ 1 keV (FWHM ≈ 2.35 keV).

IV.B. Signal and signal-to-noise ratio

The signal S of the three cavities of the simulated phantom extracted from the logarithmically subtracted images is shown in the left panel of Fig. 8 as a function of the energy smearing (Gaussian width) of the x-ray beam in the case of iodine concentration of 92 mg/ml. In the right panel of Fig. 8 the signal S of the 1 mm cavity for the three simulated iodine concentrations is displayed. The measured signals in the log-subtracted images agree with the expected values $S_{\text{theo}} = \rho_{\text{iodine}}$ (represented by the thick gray lines in Fig. 8) for x-ray energy dispersions $\sigma_{E_\gamma} \leq 1$ keV, corresponding to FWHM ≈ 2.35 keV. For larger values of energy dispersion, a decrease of the signal S with increasing σ_{E_γ} is observed. This behavior can be understood considering that, when the

x-ray energy smearing increases, the fraction of photons of the low- (high) energy beam with energy higher (lower) than the iodine K -edge also increases. These fractions are practically negligible (less than 2.4% and 0.75% for the high and low-energy beam, respectively) up to $\sigma_{E_\gamma} = 1$ keV, while they become 9.5% and 5% already at $\sigma_{E_\gamma} = 1.5$ keV.

Figure 9 shows the behavior of the signal-to-noise ratio (SNR) as a function of the x-ray energy smearing (Gaussian width) for the three cavities of the phantom in the case of iodine concentration of 92 mg/ml. The sampling area for noise is $4(2 \times 2)$ pixels, i.e., 0.2×0.6 mm². The small size of this area has been chosen in order to have a better determination of the noise thanks to a large number of samplings in the image region where only PMMA is present. The SNR of the two “base” (high-energy and low-energy) images and of the resulting subtracted image are displayed. The SNR of the subtracted image is lower than the one of the high-energy

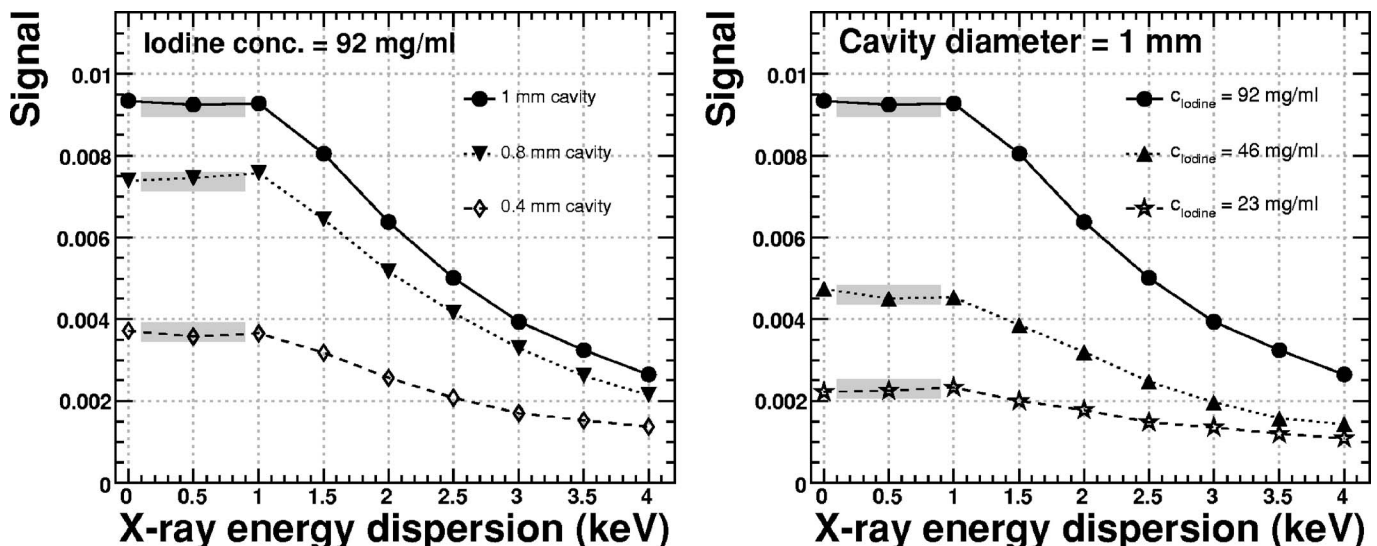


FIG. 8. Iodine signal S in the logarithmically subtracted images as a function of σ_{E_γ} for the different phantom cavities (left) and iodine concentrations (right). The thick gray lines correspond to the expected signal values ($S = \rho_{\text{iodine}}$).

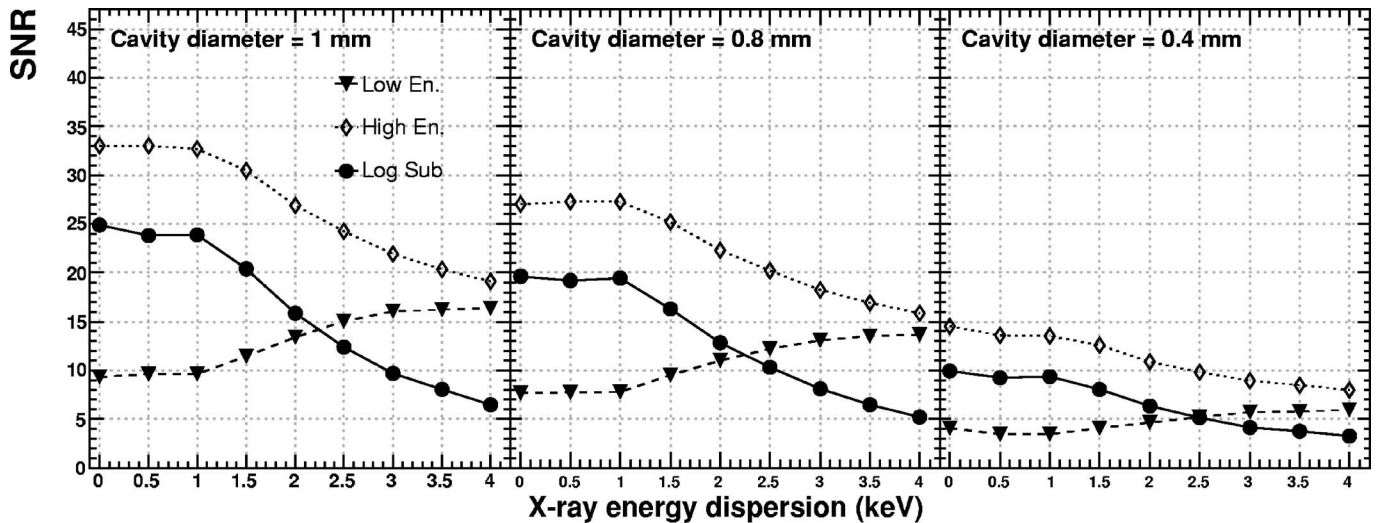


FIG. 9. SNR as a function of σ_{E_γ} for the three cavities of the simulated phantom for an iodine concentration of 92 mg/ml.

image. This is an expected result because in the subtracted image the iodine signal is practically determined by the high-energy photons (which are more absorbed by the iodine), while the noise is larger than that of the original images due to the contribution of the fluctuations of both low and high-energy images. In practice, the low-energy image allows cancellation of the background structures at the price of an increased noise in the log-subtracted image. It should be stressed that, even if the SNR in the subtracted image is lower with respect to the high-energy one, the *K*-edge technique allows one to enhance the visibility of the interesting details because the background structures are canceled in the logarithmic subtraction. Finally, one can observe in Fig. 9 that the SNR of the subtracted image results to be higher than that of the low-energy image up to a σ_{E_γ} value of about 2.5 keV.

The dependence of the SNR on the x-ray energy dispersion is similar to the one observed for the signal in Fig. 8. The SNR is practically independent of the beam energy smearing if its Gaussian width σ_{E_γ} is ≤ 1 keV (corresponding to FWHM ≈ 2.35 keV), while for larger values of energy dispersion the SNR decreases with increasing σ_{E_γ} . As already pointed out when discussing the signal in the subtracted image, the decrease of the SNR with increasing x-ray energy dispersion can be understood as a consequence of the increase in the two quasi-monochromatic beams of the contamination from photons with energy crossing the iodine *K*-edge. Finally, it can be noticed in Fig. 9 that the values of the SNR of the subtracted images scale linearly (as expected) with the tube diameter, i.e., with the iodine length traversed by the x-ray photons.

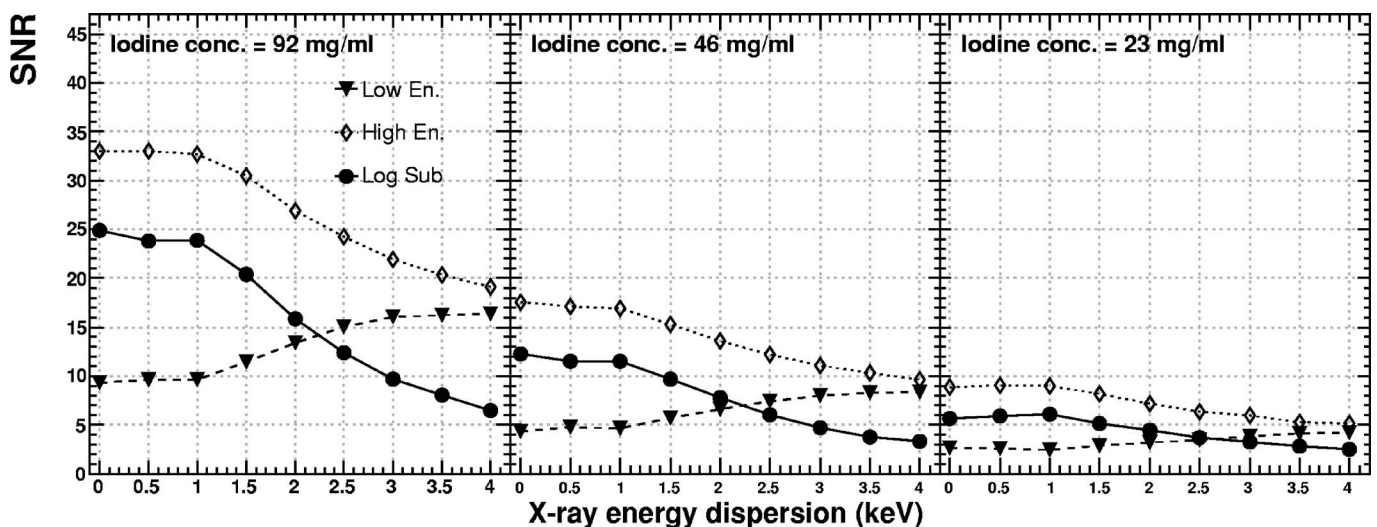


FIG. 10. SNR as a function of σ_{E_γ} for three different iodine concentrations: 92 (left panel), 46 (middle panel), and 23 (right panel) mg/ml for a tube diameter of 1 mm.

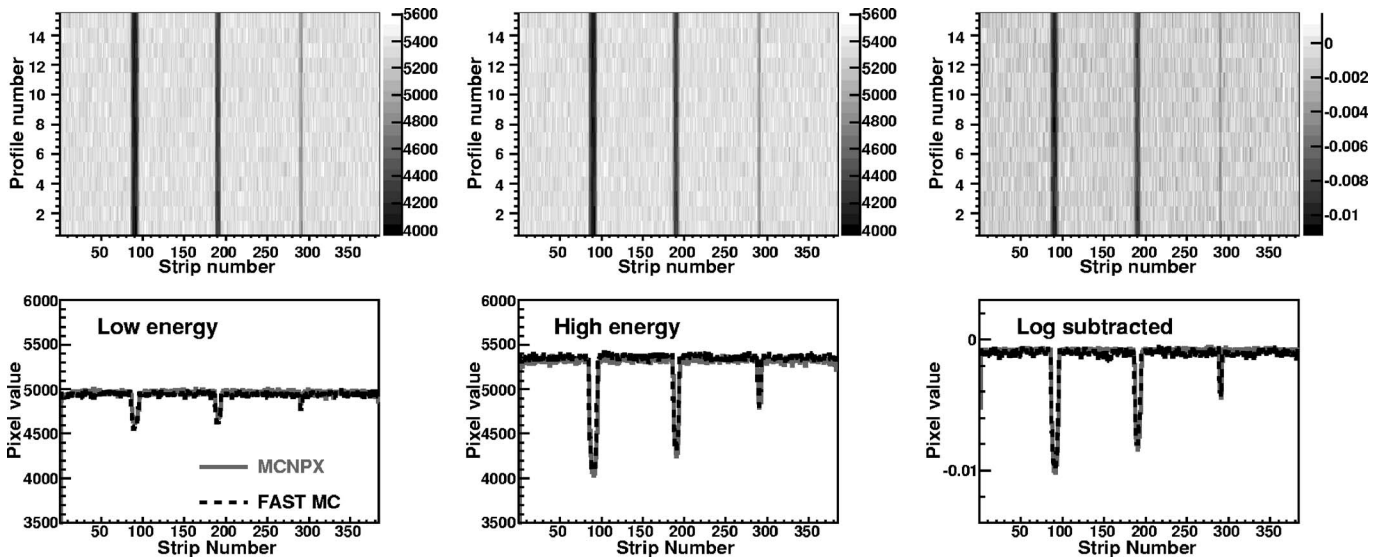


FIG. 11. Top: Low-energy (left), high-energy (middle), and log-subtracted (right) images from fast simulations of phantom absorption for iodine concentration of 92 mg/ml and $\sigma_{E_\gamma} = 1$ keV. Bottom: Average phantom profiles from fast and MCNPX simulations. The MCNPX profiles of low and high-energy images are normalized to the fast simulated ones in the PMMA regions.

The same analysis has been performed for the other two iodine concentrations (46 and 23 mg/ml). Figure 10 shows the behavior of the SNR as a function of σ_{E_γ} for the 1 mm diameter cavity and three different iodine concentrations, namely 92 (left panel), 46 (middle panel), and 23 (right panel) mg/ml. The expected linear scaling of the SNR of the logarithmically subtracted image with the iodine concentration is observed. Also in this case, the SNR is not significantly influenced by the x-ray energy smearing if $\sigma_{E_\gamma} \leq 1$ keV, and for larger dispersions it decreases with increasing σ_{E_γ} . So, if the energy dispersion exceeds 1 keV of Gaussian sigma (2.35 keV of FWHM), a higher dose is required to obtain the same SNR that would be obtained with monochromatic beams.

Finally, let us point out that the use of PMMA instead of water as a basis material has a very limited influence (less than 5%) on the values of iodine signal and SNR in the subtracted image.

IV.C. Combining beam energy separation and dispersion

The results presented in the previous paragraph have shown that for two quasi-monochromatic beams of 31.2 and 35.6 keV (i.e., energy separation of 4.4 keV) the energy dispersion of the x rays does not affect the image quality (background cancellation, signal, and SNR) if the energy smearing is characterized by a Gaussian sigma σ_{E_γ} below 1.5 keV. It is

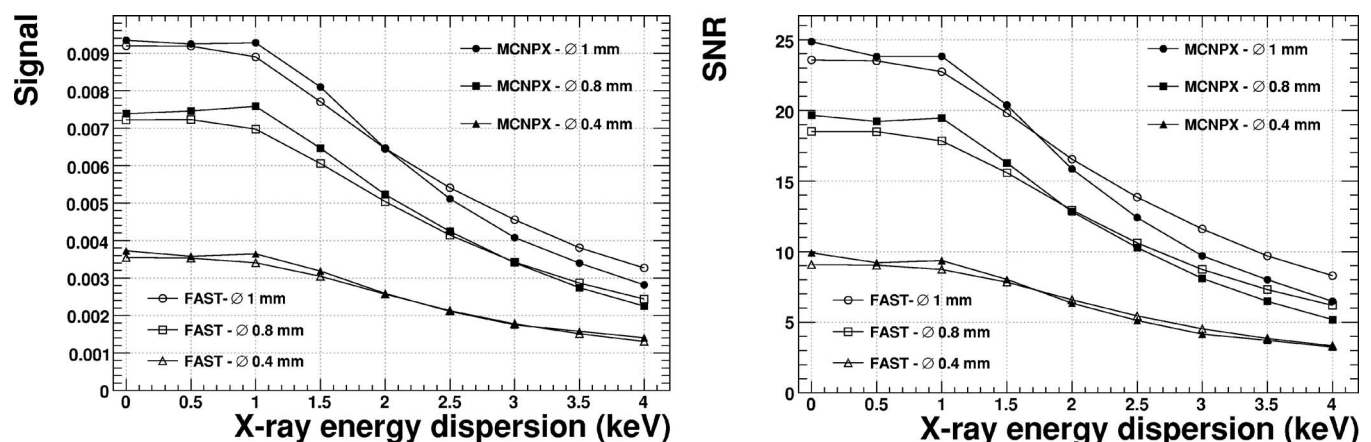


FIG. 12. Signal (left) and signal-to-noise ratio (right) as a function of x-ray energy dispersion for iodine concentration of 92 mg/ml. Results obtained with MCNPX, and fast simulations of phantom absorption are superimposed.

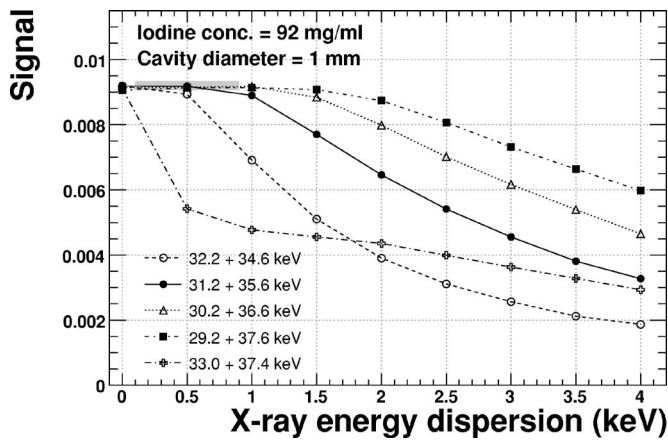


FIG. 13. Signal as a function of x-ray energy dispersion for the 1 mm diameter cavity and iodine concentration of 92 mg/ml. Results obtained with different energy pairs are superimposed.

interesting to investigate the image quality as a function of the x-ray energy smearing also for different pairs of beam energies.

This has been done by means of a C++ simulation program [using ROOT, (Ref. 19) libraries] based on the absorption coefficients of the three materials which compose the phantom used in MCNPX simulations, namely PMMA, water, and iodine (which constitute the iodate solution injected in the phantom cavities). For each photon, the energy and the position are randomly extracted using the Mersenne twister algorithm.²⁰ The x-ray position is generated with a flat distribution in a range of 4 cm along the phantom length and it is used to calculate, according to the phantom geometry described in Sec. II, the thickness of the materials (PMMA and iodate solution) traversed by that photon. The x-ray energy is generated according to a Gaussian distribution and it is used to calculate the total absorption coefficients of PMMA, water, and iodine by interpolating the values of the XCOM (Ref. 15) database. In this way, for each photon a survival probability $\exp\{-\mu/\rho\cdot\rho t\}$ is calculated and surviving photons are then counted by the corresponding pixel. An example of resulting low-energy (left), high-energy (middle), and log-subtracted (right) images is shown in the top panels of Fig.

11 for the case of 92 mg/ml iodine concentration and $\sigma_{E_\gamma} = 1$ keV. In the bottom panels of Fig. 11 the average profiles of the images in the corresponding top panels are superimposed to the ones obtained with MCNPX at the same energy smearing and iodine concentration. In order to allow for an easier comparison, the MCNPX profiles of the high and low-energy images have been normalized to the fast-simulated ones by using the counts measured in the PMMA regions of the images.

This approach resulted to be much faster than the full MCNPX simulations (about 16 s instead of ≈ 45 min to generate one profile with ≈ 5000 counts/pixel on a Pentium IV PC). Of course, these simulations are less realistic than the MCNPX ones since no transport of the photon is done, the Compton scattering is treated as if the x-ray is always completely absorbed in the phantom, and the detector response is not included. However, as it can be seen in Fig. 12, the results obtained with these simple simulations are in good agreement with the ones obtained with full MCNPX simulations for both the signal and the SNR, indicating that the most important features of the image quality can be investigated also with this simple model.

The fast simulations of phantom absorption have been run for five different energy pairs, which are reported in the legend of Fig. 13. For each energy pair, the energy smearing has been varied between 0 and 4 keV of Gaussian width with a step of 0.5 keV. The resulting iodine signals in the logarithmic subtracted image are shown in Fig. 13 as a function of the x-ray energy dispersion. It can be seen that for the four energy pairs, which are approximately symmetric about the iodine *K*-edge, the range of σ_{E_γ} where the signal remains constant (and equal to ρt) becomes larger with increasing energy separation. This is expected because, when the beam energy separation increases, also the distance of the average beam energies from the iodine *K*-edge increases and consequently the contamination in the low (high) energy beam from photons with energy above (below) the *K*-edge starts to play an important role only for larger values of energy dispersion. This is indeed confirmed by the result obtained with the 33.0–37.4 keV energy pair (cross markers in Fig. 13), which has the same energy separation $\Delta E=4.4$ keV as the

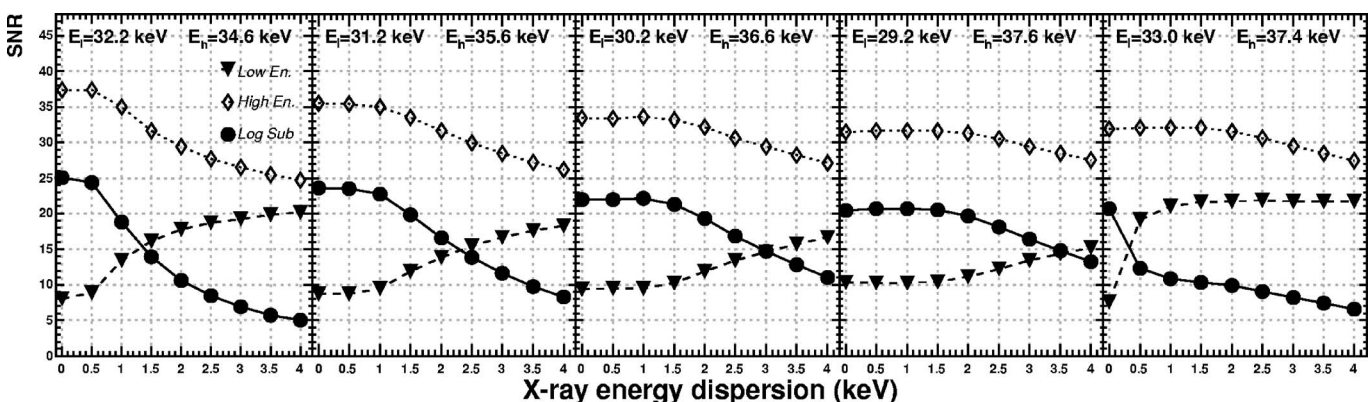


FIG. 14. SNR as a function of x-ray energy dispersion for the 1 mm diameter cavity and iodine concentration of 92 mg/ml. The five panels report the results obtained for the five different energy pairs used in the fast simulations.

31.2–35.6 pair, but the average low energy very close to the iodine *K*-edge. In this case, the signal decreases dramatically already for an energy dispersion with a Gaussian sigma of 0.5 keV (FWHM \approx 1.2 keV). As a rule of thumb, from Fig. 13 one could conclude that the signal remains practically unaffected by the energy smearing if the distance between the average energy of each of the two beams and the iodine *K*-edge is larger than about 2 Gaussian sigmas.

In Fig. 14, the SNR values of the 1 mm iodine cavity observed in the high-energy, low energy, and log-subtracted images for the five different energy pairs of Fig. 13 are shown. It can be noticed that, as already observed in Refs. 11 and 12, the increase of energy separation has a small effect on the SNR of the subtracted image, which decreases only by 20% when the energy separation is increased (by a factor of 3.5) from 2.4 to 8.4 keV. The dependence of SNR on energy dispersion confirms the conclusions drawn when discussing the iodine signal: the range where the SNR is stable against σ_{E_γ} increases with increasing distance between the beam energies and the iodine *K*-edge. Also, the σ_{E_γ} value where the SNR of the subtracted image becomes smaller than that of the low-energy one is seen to increase with increasing energy separation. The resulting SNR with the 33.0–37.4 energy pair shows that the dramatic decrease of image quality at $\sigma_{E_\gamma} = 0.5$ keV is a consequence of the simultaneous jump of the low-energy image SNR due to the fact that 37% of the x rays in the low-energy beam are above the *K*-edge and suffer stronger absorption by the iodine. The combined dependence of SNR on energy separation and energy dispersion indicates that a larger separation between the average beam energies and the iodine *K*-edge allows for a larger tolerable energy dispersion at the price of a small decrease of the SNR.

V. CONCLUSIONS

In this paper, we have studied *K*-edge subtraction technique as a way of improving the detail visibility by subtracting two images obtained with quasi-monochromatic x-ray beams at two different energies bracketing the iodine *K*-edge. Monte Carlo simulations of the images of a simple phantom with cylindrical cavities simulating patient vessels have been performed to investigate the effect of the energy dispersion of the x-ray beams. This energy dispersion is negligible in the case of x-ray beams from synchrotrons, but it is potentially important in the case of compact sources like the one described in Ref. 7. The results presented in this paper show that even if the “base” (high-energy and low-energy) images are not obtained with truly monochromatic beams, the resulting subtracted images still have a quality compatible with the one that would be obtained with perfectly monochromatic beams up to a certain value of x-ray energy dispersion. This limiting dispersion value is found to depend on the distance between the average energy of each beam and the iodine *K*-edge. The maximum tolerable energy dispersion can be estimated as one half of the distance between the average beam energy and the *K*-edge, so that the contamination in the low- (high) energy beam from photons with energy above(below) the *K*-edge is kept below \approx 2%. For

larger energy dispersions, a larger dose is required to obtain the same SNR that would be obtained with monochromatic beams. Furthermore, for energy dispersions below the mentioned limit the background cancellation is found to be effective and the iodine signal in the logarithmically subtracted image results to be equal to the thickness ρt of the contrast medium. The characteristics of the quasi-monochromatic beams produced with a conventional x-ray tube and a mosaic crystal monochromator described in Ref. 7 with average energies of 31.2 and 35.6 keV fulfill this condition. Finally, let us point out that the results of this simulation work may also be useful for the design and the optimization of quasi-monochromatic x-ray sources. For example, the geometry of the collimator can be tuned so as to obtain the maximum tolerable energy dispersion for a given energy pair, thus maximizing the photon flux and reducing the imaging time.

ACKNOWLEDGMENTS

The authors are grateful to Juan Antonio Rubio for allowing the use of the CIEMAT computing cluster for the simulation work presented in this article. This work was supported in part by the TRIL program from ICTP Trieste.

^{a)}Electronic mail: prino@to.infn.it

¹B. Jacobson, “Dichromatic absorption radiography-dichromography,” *Acta Radiol.* **39**, 437–452 (1953).

²W. R. Dix *et al.*, “Comparison of intravenous coronary angiography using synchrotron radiation with selective coronary angiography,” *J. Synchrotron Radiat.* **10**, 219–227 (2003).

³B. Bertrand *et al.*, “Comparison of synchrotron radiation angiography for the diagnosis of in-stent restenosis after percutaneous transluminal coronary angioplasty,” *Eur. Heart J.* **26**, 1284–1291 (2005).

⁴E. Schultke *et al.*, “The potential for neurovascular intravenous angiography using k-edge digital subtraction angiography,” *Nucl. Instrum. Methods Phys. Res. A* **548**, 84–87 (2005).

⁵M. Skarpathiotakis *et al.*, “Development of contrast digital mammography,” *Med. Phys.* **29**, 2419–2426 (2002).

⁶J. M. Lewin *et al.*, “Dual-energy contrast enhanced digital subtraction mammography: Feasibility,” *Radiology* **229**, 261–268 (2003).

⁷M. Gambaccini *et al.*, “Narrow energy band X-rays via mosaic crystal for mammography application,” *Nucl. Instrum. Methods Phys. Res. A* **365**, 248–254 (1995).

⁸M. Gambaccini *et al.*, “Spatial resolution measurements in quasimonochromatic x rays with mosaic crystals for mammography application,” *Med. Phys.* **28**, 412–418 (2001).

⁹A. Sarnelli *et al.*, “K-edge digital subtraction imaging based on a dichromatic and compact x-ray source,” *Phys. Med. Biol.* **49**, 3291–3305 (2004).

¹⁰C. Ceballos *et al.*, “Monte Carlo simulation of a silicon strip detector for angiography applications. First approach,” *AIP Conf. Proc.* **682**, 185–191 (2003).

¹¹A. Sarnelli *et al.*, “K-edge digital subtraction imaging with dichromatic x-ray sources: SNR and dose studies,” *Phys. Med. Biol.* **51**, 4311–4328 (2006).

¹²A. Sarnelli *et al.*, “Quantitative analysis of the effect of energy separation in k-edge digital subtraction imaging,” *Phys. Med. Biol.* **52**, 3015–3026 (2007).

¹³MCNP 4C-Monte Carlo N-Particle Transport Code System,” RSICC Computer Code Collection, Oak Ridge National Laboratory (2001).

¹⁴C. Avila *et al.*, “Contrast cancellation technique applied to digital x-ray imaging using silicon strip detectors,” *Med. Phys.* **32**, 3755–3766 (2005). <http://physics.nist.gov/physrefdata/xcom/text/xcom.html>

¹⁵S. Molloy *et al.*, “Quantification of coronary arterial calcium by dual energy digital subtraction fluoroscopy,” *Med. Phys.* **18**, 295–298 (1991).

¹⁶R. E. Alvarez and A. Macovski, “Energy-selective reconstruction in X-ray computerized tomography,” *Phys. Med. Biol.* **21**, 733–744 (1976).

¹⁸L. A. Lehmann *et al.*, "Generalized image combinations in dual KVP digital radiography," *Med. Phys.* **8**, 659–667 (1981).

¹⁹<http://root.cern.ch>

²⁰M. Matsumoto and T. Nishimura, "Mersenne twister: A 623-dimensionally equidistributed uniform pseudo-random number generator," *ACM Trans. Model. Comput. Simul.* **8**, 3–30 (1998).